





Cite this: *Soft Matter*, 2025,  
21, 7125

Received 20th May 2025,  
Accepted 14th August 2025

DOI: 10.1039/d5sm00525f

[rsc.li/soft-matter-journal](https://rsc.li/soft-matter-journal)

# Iso- to anisotropic wetting on microwrinkled surfaces with varying intrinsic wettability

Hisay Lama,  Hui Mao and João T. Cabral  \*

We examine the combined effects of topography and intrinsic material wettability on the overall wetting behaviour of patterned surfaces, with widespread practical applications. While the presence of surface microwrinkles is well-known to induce anisotropic wetting, we experimentally map the relation between the degree of anisotropy and the intrinsic wettability of the surface. We employ one-dimensional (1D) wrinkling of polydimethylsiloxane (PDMS) elastomers, with tuneable periodicity and amplitude, and separately vary the intrinsic contact angle by controlled surface oxidation and hydrophobic recovery. We demonstrate the importance of the interplay between topography and intrinsic wetting by switching the spontaneous, gravity-driven droplet motion on vertically inclined representative surfaces. We describe our findings with a minimal model that estimates the threshold volume necessary for the droplet mobility on a vertically inclined surface. These findings provide a framework for designing surfaces that support the passive, self-cleaning of functional coatings.

## 1 Introduction

Self-cleaning of liquid droplets from functional surfaces, including windows, solar panels, coatings and textiles,<sup>1–5</sup> presents a considerable challenge due to liquid–solid adhesion and the dominance of capillary forces. Conversely, the retention of liquid droplets, for instance containing agrichemicals employed in crop protection or fertilisation, or in various printing applications, is often problematic, partly due to gravity-induced effects and roll off.<sup>6</sup> Designing surfaces to facilitate either retention or passive removal of a liquid drop is thus essential to deliver their practical utility and performance.<sup>3,4,7,8</sup>

Common strategies to promote droplet removal include fabricating surface microstructures that function as rails and enable passive and directional droplet transport along defined pathways,<sup>9–12</sup> or designing bioinspired microstructures that can induce superhydrophobicity through prescribed ‘roughness’.<sup>13,14</sup> In contrast, to enhance droplet retention, lyophilic surfaces are desirable,<sup>15</sup> whereas maintaining lyophilicity while achieving self-cleaning functionality is advantageous in several practical applications.<sup>4,5,16</sup> It is therefore important to understand the combined effects of roughness and intrinsic material wettability on surface wetting and their impact on droplet dynamics on surfaces.

Beyond droplet removal and retention, rough or micro-patterned surfaces find numerous applications, including promoting droplet coalescence,<sup>4,5</sup> enabling liquid lithography,<sup>17,18</sup> facilitating

contaminant removal,<sup>19–21</sup> supporting biological assays<sup>22,23</sup> and colloidal coating,<sup>24,25</sup> and enabling switchable wettability.<sup>26</sup>

In general, liquid droplets on surfaces with micropattern-induced roughness exhibit static contact angles that differ from their intrinsic contact angles (*i.e.*, those without any micropattern).<sup>6,15,27–31</sup> In simple terms, roughness on surfaces ‘amplifies’ wettability, by reducing the contact angle on lyophilic surfaces and increasing it on lyophobic ones.<sup>6,15,27,29,30</sup> When such roughness is anisotropic, as in the case of a surface with one-dimensional (1D) microwrinkles, sessile water droplets exhibit *anisotropic wetting* accompanied by orientation-dependent contact angles.<sup>32–34</sup> This leads to asymmetry in the droplet base radii, which are elongated along the wrinkle orientation and shortened in the perpendicular direction. The extent of anisotropy in the surface wetting varies as a function of the wrinkling periodicity and amplitude, leading to a transition in droplet shape from circular to elongated.<sup>34</sup>

In this paper, we examine how the intrinsic contact angle of a liquid on microwrinkled surfaces influences the shape and the effective wettability of a sessile droplet, corresponding contact angles, and its effect on droplet mobility. We conducted model experiments using water as the testing liquid and a polydimethylsiloxane (PDMS) substrate engineered with sinusoidal microwrinkles, resembling 1D roughness, with tunable amplitude and periodicity. The intrinsic contact angle of water droplets on these PDMS surfaces was systematically adjusted by modifying the surface free energy by controlled plasma oxidation and hydrophobic recovery.

Our investigation revealed that the anisotropic wetting of water droplets on surfaces with 1D roughness arises not only

Department of Chemical Engineering, Imperial College London, London SW7 2AZ, UK. E-mail: [j.cabral@imperial.ac.uk](mailto:j.cabral@imperial.ac.uk)



from the anisotropic surface features (sinusoidal wrinkles), but is also governed by the intrinsic liquid–solid contact angle. We map their interdependencies and present them as a function of variations in droplet shape anisotropy. We observe that on surfaces with higher surface wettability, corresponding to lower intrinsic liquid–solid contact angles  $\sim 44^\circ$ , the water droplet footprint extends preferentially along the wrinkle direction, resulting in an anisotropic wetting with a droplet elongated shape. In contrast, on low-energy surfaces, with  $\sim 110^\circ$ , the droplet maintains a circular footprint, resulting in an isotropic wetting, as the solid–liquid–air contact line cannot deform significantly and the static contact angle remains uniform across the droplet periphery. This contrasting behaviour is observed to directly influence droplet mobility on vertically inclined rough surfaces, especially when the wrinkles are aligned with the direction of gravitational acceleration. To explain the directional motion of droplets, we developed a minimal model that balances gravitational forces with capillary adhesion and interfacial damping. The model corroborates our experimental findings by showing that the damping force is reduced along the wrinkle direction for elongated droplets compared to circular ones, leading to enhanced droplet velocity in that direction.

## 2 Experimental methodology

### 2.1 Fabrication and characterisation of 1D roughness

The complete process outlining the different stages of the fabrication of the test surface is illustrated in Fig. 1(a), which involves (i) the fabrication of polydimethylsiloxane (PDMS) mold, (ii) the generation of one-dimensional (1D) microwrinkles, serving as a model for the 1D surface roughness, and (iii) replicating the 1D roughness on fresh PDMS, to ensure uniform mechanical properties across the material. Each of these stages is described in detail below:

(i) Fabrication of the PDMS mold: the process of preparing the PDMS mold is as follows – first, in a plastic cup, we mix the base and crosslinker of Sylgard 184 (Dow Corning, USA) in a 10 : 1 weight ratio. The mixture is then stirred with a spatula for 5 minutes, during which bubbles are generated. These bubbles were subsequently eliminated through degassing the mixture in a vacuum desiccator for approximately 45 minutes. Once fully degassed, we cast the mixture into a Petri dish and cure it at  $75^\circ\text{C}$  for 1 h, yielding a PDMS mold of thickness 1.4 mm. The cured film is then cut into rectangular pieces measuring  $60\text{ mm} \times 30\text{ mm}$  in length and width, respectively.

(ii) Generation of surface microwrinkles: we first load the rectangular-shaped PDMS mold onto a custom-built strain

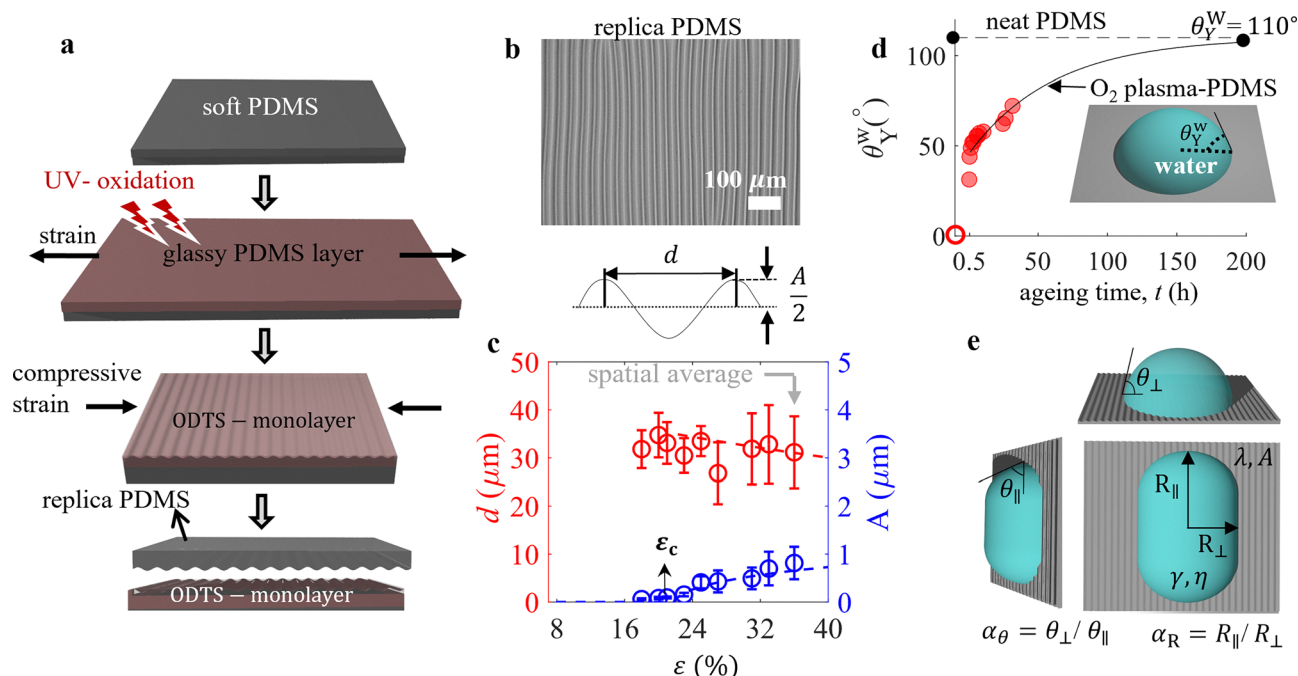


**Fig. 1** Fabrication and characterisation of one-dimensional (1D) wrinkled surfaces and their surface wettability properties. (a) Schematic of the fabrication process, from top to bottom: soft PDMS, uniaxially stretched and exposed to UV-radiation forms a stiff, glassy surface layer; upon strain release, compression induces linear (or 1D) surface wrinkles with prescribed amplitude and periodicity. A monolayer of ODTs is deposited on the wrinkled PDMS, followed by casting and replication the 1D wrinkled structure onto fresh PDMS. (b) Microscopy image of a representative wrinkled PDMS replica with linear surface wrinkles formed at a compressive strain of  $\epsilon = 36\%$  and 60 min UVO exposure. (c) Wrinkle periodicity  $d$  (left axis, red) and amplitude  $A$  (right axis, blue) as a function of applied compressive strain  $\epsilon$ , and corresponding model predictions,<sup>35</sup> with critical strain  $\epsilon_c = 22\%$  marking the onset of wrinkling. We discuss the details on spatial average in the SI (see Fig. S1). (d) Surfaces with varying intrinsic water contact angle ( $\theta_Y^w$ ): temporal evolution of the water contact angle  $\theta_Y^w$  on oxygen plasma-treated PDMS, showing hydrophobic recovery approaching the neat PDMS value ( $\theta_Y^w \approx 110^\circ$ ). The solid line approaching  $110^\circ$  is a guide to the eye. The red circle at the origin represents  $t = 0$  h. (e) Schematic of the sessile droplet configuration on 1D wrinkled surface, illustrating orientation-dependent contact angles ( $\theta_\perp, \theta_\parallel$ ) and base radii ( $R_\perp, R_\parallel$ ). The respective anisotropy ratios are defined as  $\alpha_\theta \equiv \theta_\perp / \theta_\parallel$  and  $\alpha_R \equiv R_\perp / R_\parallel$ .



stage and apply a uniaxial strain. We subject the stretched PDMS to UV ozonolysis (Novoscan, PSD Pro Series, USA), maintaining the surface-to-lamp distance of 8 mm for 60 min, forming a glassy skin layer atop a soft PDMS elastomer substrate, well documented in the literature.<sup>36–41</sup> After UV exposure, we slowly release the pre-applied strain, compressing the PDMS mold with a compressive strain ( $\varepsilon$ ) ranging from 5% to 36%. This compression induces the 1D linear microwrinkles on the PDMS surface, characterised by a wrinkling periodicity  $d$  and amplitude  $A$ .

(iii) Replica PDMS surface: the UV-oxidation used to generate one-dimensional microwrinkles on the PDMS mold, forming a glassy skin layer, which can create mechanical heterogeneity on the surface and hinder the accurate wettability measurements. To ensure mechanical homogeneity, we prepared a replica of PDMS, copying the fabricated pattern. We employed an imprinting lithography technique<sup>42</sup> to fabricate the fresh PDMS replica surface featuring the 1D microwrinkles. Note that the fabrication of micron-wrinkles on the PDMS surface through UV-oxidation makes the surface hydrophilic, reducing the intrinsic contact angle to approximately  $62^\circ$ , which complicates the imprinting lithography process. The post-imprinting stage becomes difficult as we cannot separate the microwrinkled PDMS from the replica PDMS. To address this, we first deposited a self-assembled monolayer of octadecyltrichlorosilane (ODTS) to make the wrinkled PDMS surface hydrophobic. The self-assembled monolayer of ODTS was obtained through exposing the PDMS (UV-oxidised wrinkled surface) to the vapour of ODTS for 40 minutes. We then used this modified wrinkled surface as the imprinting stamp, cast uncured PDMS (10:1) onto it, and cured the assembly at  $75^\circ\text{C}$  for 1 h. After curing, we separated the PDMS from the stamp, successfully transferring the microwrinkled pattern onto the bottom surface of the replica PDMS. We measured the amplitude and periodicity of the microwrinkles from the surface height profile obtained using the Bruker DektakXT profilometer. The surface height profile data were analysed using Gwyddion.

## 2.2 Quantification of microwrinkles

We measured the mean values of wrinkle periodicity ( $d$ ) and amplitude ( $A$ ) of sinusoidal microwrinkles that create the 1D roughness on the PDMS surface, across various locations on the surface from the surface profiles. These values are plotted as a function of compressive strain ( $\varepsilon$ ) as shown in Fig. 1(c). On increasing  $\varepsilon$ , the mean periodicity  $d$  remains nearly constant, while the mean amplitude  $A$  increases with  $\varepsilon$ . The onset of wrinkling instability is observed at  $\varepsilon = \varepsilon_c = 22\%$ . From Fig. 1(c), the periodicity  $d$  remains nearly constant while the amplitude  $A$  increases with increasing  $\varepsilon$ , henceforth, we use  $A$  as a representative parameter to quantify the 1D surface roughness of the PDMS. The larger errorbar in  $d$  at high compressive strain is attributed to the spatial heterogeneity in  $d$  when averaged over a sample size of  $1\text{ mm} \times 1\text{ mm}$  (see Fig. S1).

We characterise these sinusoidal microwrinkles using two key parameters, wrinkle periodicity ( $d$ ) and amplitude ( $A$ ), analysed with the wrinkling framework at high deformations,<sup>35</sup>

$$d = \frac{2\pi h_f (\bar{E}_f / 3\bar{E}_s)^{1/3}}{(1 + \varepsilon)(1 + \Xi)^{1/3}} \quad (1)$$

$$A = \frac{h_f (\varepsilon / \varepsilon_c - 1)^{1/2}}{\sqrt{1 + \varepsilon}(1 + \Xi)^{1/3}} \quad (2)$$

where  $f$  and  $s$  refer to the glassy film and the substrate, respectively;  $\Xi = 5\varepsilon(1 + \varepsilon)/32$  accounts for the nonlinearity in stress and strain behaviour,  $h_f$  is the thickness of the glassy film, and  $\bar{E} = E/(1 - \nu^2)$  is plane strain Young's modulus, where  $\nu$  is Poisson ratio and  $E$  is the Young's modulus. The critical strain threshold  $\varepsilon_c = -\frac{1}{4}(3\bar{E}_s/\bar{E}_f)^{2/3}$  is the minimum strain required to excite the wrinkling instability.

UV oxidation of PDMS is known to generate a complex interfacial skin profile,<sup>37,43</sup> which does not strictly conform to a sharp bilayer (comprising a glassy skin and elastomeric substrate with a sharp interface) model. However, from a practical viewpoint, the simple bilayer model provides a descriptive framework for our wrinkling data, parameterised by  $h_f = 0.1\text{ mm}$ , and plane strain Young's modulus  $\bar{E}_f = 450\text{ MPa}$  (treated as self-consistent fitting parameters for  $d$  and  $A$  profiles), and obeying  $h_s \gg h_f$ . We used the low deformation estimate of  $d$  ( $d \rightarrow d|_{\varepsilon \rightarrow \varepsilon_c}$ ) to estimate  $\bar{E}_f$ , as in this limit, both  $d$  and  $E_f$  are approximately a constant.  $\bar{E}_f$  was estimated using the expression,  $d = 2\pi h_f (\bar{E}_f / 3\bar{E}_s)^{1/3}$ , equivalently,  $\bar{E}_f = 3\bar{E}_s \times (d_{\text{mean}} / 2\pi h_f)^3$ , with  $d_{\text{mean}} = 32\text{ }\mu\text{m}$  and  $E_s = 1\text{ MPa}$ . Under high deformations, surface wrinkles can evolve into more complex mechanical features such as folds, period-doubling patterns, and ridges. However, the overlap between experimental data and model indicates the validity of the high deformation approximation. The  $d$ - $A$  profile in Fig. 1(c) serves thus as a reliable calibration curve to tune the amplitude of microwrinkles, and therefore the surface roughness, by modulating the compressive strain.

## 2.3 Intrinsic wettability

We investigate the wettability of PDMS surfaces by measuring water-droplet contact angles in a sessile drop configuration using a drop shape analyser (DSA25S, Krüss, Germany), as shown in the inset of Fig. 1(d). We measure the intrinsic surface wettability, a key physical property that reflects a surface's affinity for liquid. It is quantified by the contact angle of a liquid droplet on a smooth or nearly smooth test surface, with  $A \approx 0$ , often called Young's contact angle in the literature.<sup>15,28,31</sup> Here it is referred to as  $\theta_Y^W$ . The neat PDMS surface, *i.e.*, the surface without any treatment and  $A \approx 0$ , we measured intrinsic water-PDMS contact angle,  $\theta_Y^W = 110^\circ$ . To obtain the PDMS with varying  $\theta_Y^W$ , we modified the PDMS surface through surface oxidation with  $\text{O}_2$  plasma (Diener Femto, Germany) at  $100\text{ W}$  and  $0.5\text{ mbar}$  pressure for 5 seconds, followed by controlled ageing. Immediately after plasma treatment, the surfaces became highly hydrophilic; however, as the surfaces aged, the wettability gradually decreased. As shown in Fig. 1(d), the intrinsic contact angle on smooth PDMS surfaces ( $A = 0$ ) increased from  $44^\circ$  (measured at  $0.5\text{ h}$ ) to  $62^\circ$  (measured at  $36\text{ h}$ ) with ageing. To obtain the microwrinkled surfaces with different intrinsic  $\theta_Y^W$ , we followed the same protocol, which is surface oxidation followed by hydrophobic recovery.<sup>38</sup>



## 2.4 Effective wettability with 1D microwrinkles

In principle, surfaces with higher roughness, *i.e.*,  $A > 0$ , effective wettability is described by the apparent (or experimental) contact angle ( $\theta$ ), which typically differs from the intrinsic contact angle ( $\theta_Y^W$ ). To study how the intrinsic contact angle affects the surface wrinkles-driven wettability of PDMS surfaces with one-dimensional (1D) microwrinkles, we prepared 1D microwrinkled surfaces with varying intrinsic contact angles ( $\theta_Y^W$ ). We performed the wettability measurements with the drop in sessile drop configuration, then recording the apparent contact angles and measuring the droplet radii along two orthogonal directions relative to the wrinkle orientation: parallel ( $\theta_{\parallel}$ ,  $R_{\parallel}$ ) and perpendicular ( $\theta_{\perp}$ ,  $R_{\perp}$ ). The static droplet shapes on the microwrinkled surfaces were characterised using two anisotropy parameters: the droplet shape anisotropy,  $\alpha_R = R_{\parallel}/R_{\perp}$ , and the contact angle anisotropy,  $\alpha_{\theta} = \theta_{\perp}/\theta_{\parallel}$ . Note that the apparent contact angles  $\theta_{\perp}$  and  $\theta_{\parallel}$  were measured using a drop shape analyser (DSA25S, Krüss), while the droplet radii  $R_{\parallel}$  and  $R_{\perp}$  were extracted from top-view microscopy images using appropriate thresholding and binarisation techniques in MATLAB. Note that the microscopy images were taken with a  $5\times$  objective (N.A. = 0.10) of an Olympus BX41M microscope equipped with a Basler camera (Basler-aca 2000 – 165uc, Germany).

## 3 Results

### 3.1 Surface microwrinkle induced droplet shape anisotropy

#### 3.1.1 Evolution of droplet shape: from circular to elongated.

We first examine how the shape of a sessile droplet changes on surfaces with varying magnitudes of one-dimensional (1D) microwrinkles, characterised by amplitude  $A$ , and different intrinsic water contact angles  $\theta_Y^W$ . Although it is well-established that 1D topographical features generally induce elongation of water droplets along the direction of the wrinkles,<sup>34</sup> we evaluate how this behaviour is modulated by intrinsic contact angle,  $\theta_Y^W$ . To explore this, we examine the influence of microwrinkle amplitude  $A \in [0, 0.81 \mu\text{m}]$  and intrinsic contact angle  $\theta_Y^W \in [44^\circ, 110^\circ]$  on the shape of a  $2 \mu\text{L}$  water droplet in a sessile configuration on PDMS surfaces with various combinations of  $A$  and  $\theta_Y^W$ . The sessile drop shape anisotropy is quantified by  $\alpha_R$ , which is the ratio of drop's base radii measured along parallel and perpendicular to the wrinkle orientation. Fig. 2(a) presents a matrix of top-view microscopy images of the droplets, with  $A$  and  $\theta_Y^W$  varying along the horizontal and vertical axes, respectively.

At the lower end of the apparent contact angle range investigated,  $\theta_Y^W = 44^\circ$ , the droplet shape transitions from circular to an elongated shape as  $A$  increases from 0 to  $0.81 \mu\text{m}$ , with noticeable non-circularity in droplet shape, appearing at  $A \geq 0.15 \mu\text{m}$  and reaching a maximum elongation at  $A = 0.81 \mu\text{m}$ . In contrast, at  $\theta_Y^W = 110^\circ$ , the droplet maintains a circular shape across all tested values of  $A$ . For intermediate  $\theta_Y^W$ , the transition from circular to elongated shapes still occurs with increasing  $A$ , but the onset of droplet shape-anisotropy shifts to the right towards higher values of  $A$  on increasing  $\theta_Y^W$ . For all  $\theta_Y^W$ , except at  $\theta_Y^W = 110^\circ$  the degree of shape anisotropy is consistently highest

at  $A = 0.81 \mu\text{m}$ . Besides, it is apparent from Fig. 2(a), we can map the droplet shape anisotropy with  $\theta_Y^W$  and  $A$ . Accordingly, we present a corresponding heat map in Fig. 2(b), where the colour (dark brown to yellow) represents the degree of droplet shape anisotropy, quantified by  $\alpha_R$  ( $R_{\parallel}/R_{\perp}$ ). Based on the microscopy images in Fig. 2(a), droplets with  $\alpha_R < 1.2$  are considered approximately circular, with  $R_{\parallel} \simeq R_{\perp}$ . Droplets with  $\alpha_R > 1.3$  are clearly elongated, characterised by  $R_{\parallel} > R_{\perp}$ , while droplets with  $1.2 < \alpha_R < 1.3$  show moderate elongation, where  $R_{\parallel}$  is noticeably but not vastly larger than  $R_{\perp}$ . The regions I, II and III corresponding to three different  $\alpha_R$  ranges are labelled and portrayed by dashed lines in Fig. 2(b). Enlarged microscopy images representing typical droplet shapes in regions I, II, and III are shown in Fig. 2(c). For substrates with  $A = 0.81 \mu\text{m}$  and the intrinsic contact angle as low as  $35^\circ$ , the droplet becomes highly elongated, exhibiting imbibition into the microwrinkle troughs, spontaneously resulting in a filament-like morphology, as illustrated in Fig. S2. These filament kinetics were found to follow a square-law dependence between the length of the liquid filament and time, following Washburn's law.<sup>44</sup>

**3.1.2 Correlation between contact angle anisotropy and droplet shape.** To rationalise the microscopy observations presented in Fig. 2(a) and (c) as well as the heatmap shown in Fig. 2(b), we examine the droplet shapes at the extremes, specifically at the lowest and highest tested values of  $A = 0, 0.81 \mu\text{m}$  and  $\theta_Y^W = 44^\circ, 110^\circ$ , respectively. Under these conditions, we plot the droplet shape anisotropy  $\alpha_R \equiv \alpha_R(A, \theta_Y^W)|_{\theta_Y^W=44^\circ, 110^\circ}$  as a function of  $A$ , and  $\alpha_R \equiv \alpha_R(A, \theta_Y^W)|_{A=0, 0.81 \mu\text{m}}$  as a function of  $\theta_Y^W$ , shown in Fig. 3(a) and (b), respectively.

From Fig. 3(a), at  $\theta_Y^W = 44^\circ$ , the shape-anisotropy ratio  $\alpha_R$  increases nonlinearly from 1.0 to 1.5 on increasing  $A$ , indicating that the droplet shape gradually becomes more elongated as the wrinkling amplitude increases. In contrast, at  $\theta_Y^W = 110^\circ$ ,  $\alpha_R$  remains nearly constant around 1.0 across all tested  $A$ , indicating that the droplet maintains a nearly circular shape regardless of wrinkling amplitude. Next, from Fig. 3(b), we observe that the shape-anisotropy ratio,  $\alpha_R$  decreases with  $\theta_Y^W \rightarrow 110^\circ$  at  $A = 0.81 \mu\text{m}$ , while it remains constant and close to 1.0 (ideal circle) at  $A = 0$  irrespective of  $\theta_Y^W \rightarrow 110^\circ$ . Therefore, the 1D microwrinkles on the PDMS surface break circular symmetry of the droplet contact line (forming an elongated shape) when surfaces are hydrophilic, *i.e.*, low intrinsic water-PDMS contact angle with  $\theta_Y^W < 100$ . For a smooth surface, the droplet remains circular, irrespective of microwrinkle amplitude, keeping the  $\alpha_R$  ( $\approx 1$ ) constant. We tested the droplet circularity for a microwrinkled surface with  $\theta_Y^W = 110^\circ$  the droplet volume varying from 1–9  $\mu\text{L}$  (see Fig. S3). In addition, we measured the apparent contact angles ( $\theta_{\parallel}$ ,  $\theta_{\perp}$ ) with 2  $\mu\text{L}$  sessile water droplets on surfaces with microwrinkles and subsequently calculated the contact angle anisotropy,  $\alpha_{\theta}(\theta_{\perp}/\theta_{\parallel})$ . Following the approach used for  $\alpha_R$ , we plot the contact angle anisotropy  $\alpha_{\theta} \equiv \alpha_{\theta}(A, \theta_Y^W)|_{\theta_Y^W=44^\circ, 110^\circ}$  as a function of  $A$ , and  $\alpha_{\theta} \equiv \alpha_{\theta}(A, \theta_Y^W)|_{A=0, 0.81 \mu\text{m}}$  as a function of  $\theta_Y^W$ . The trend observed in  $\alpha_{\theta}$  is similar to that of  $\alpha_R$ , indicating that the anisotropy in the shape of the drop is followed by the





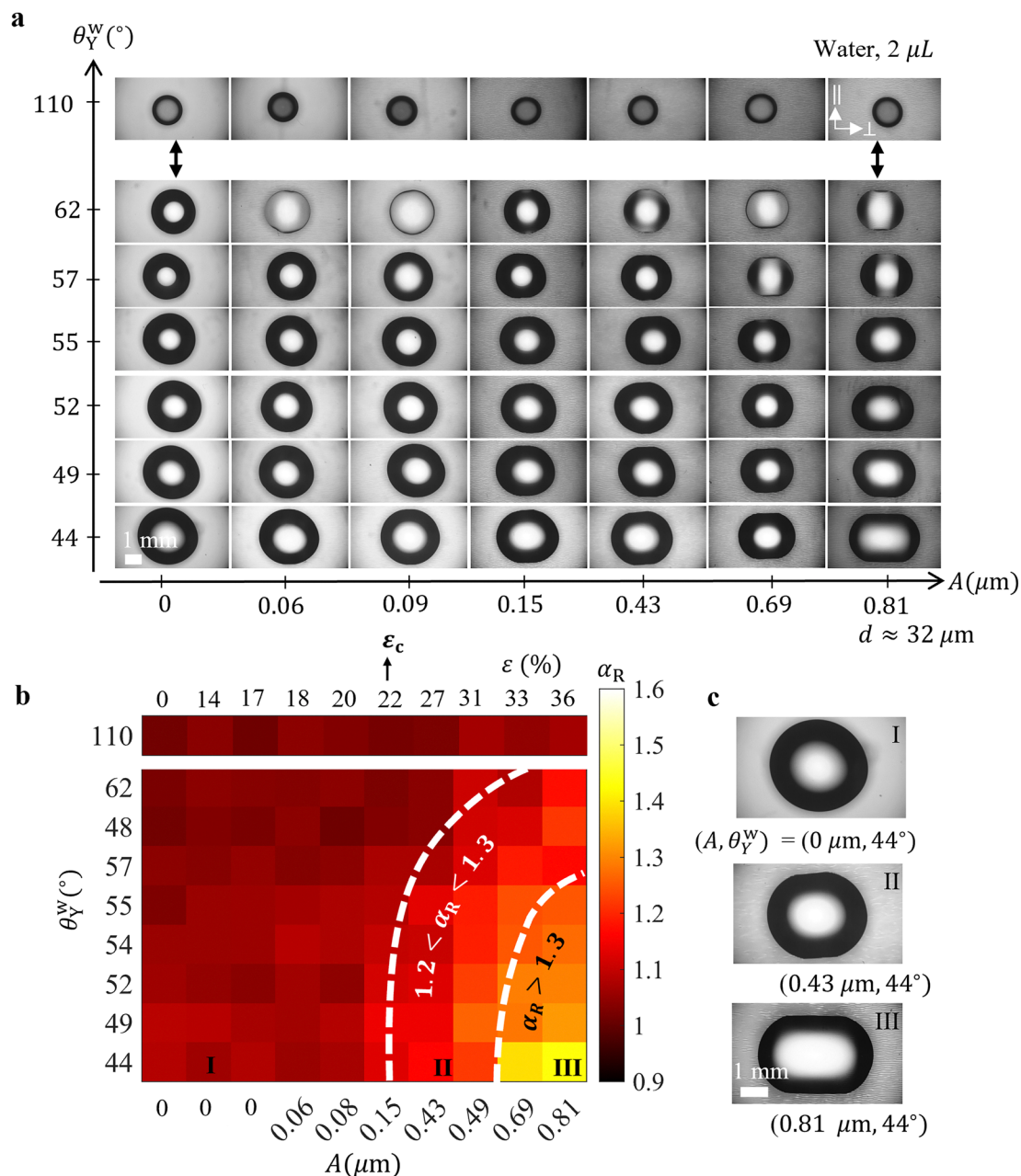


**Fig. 2** Base shape of sessile water droplets on PDMS surfaces with 1D roughness as a function of intrinsic contact angle and pattern amplitude. (a) A series of optical microscopy images showing top views of 2  $\mu\text{L}$  water droplets with intrinsic contact angles  $\theta_Y^W \in [44^\circ, 110^\circ]$  and amplitudes  $A \in [0, 0.81] \mu\text{m}$ , on surfaces with linear wrinkle spacing  $d \approx 32 \mu\text{m}$ . (b) Heat map showing the variation in droplet shape anisotropy  $\alpha_R = R_{||}/R_{\perp}$  as a function of intrinsic contact angle  $\theta_Y^W$  (left axis) and roughness amplitude  $A$  (bottom axis), with the corresponding applied strain  $\epsilon$  indicated on the top axis. The colour scale represents the magnitude of  $\alpha_R$ , and the critical strain  $\epsilon_c$  marking the onset of wrinkling is highlighted. Dashed lines demarcate distinct regimes: circular droplets (I) with  $\alpha_R < 1.2$ , moderately acircular droplets (II) with  $1.2 < \alpha_R < 1.3$ , and highly anisotropic droplets (III) with  $\alpha_R > 1.3$ . The dashed line is a guide to the eye intended to distinguish different regimes of droplet wettability. (c) Representative microscopy images showing top views of droplets corresponding to regimes I, II, and III, respectively.

anisotropy in the apparent contact angles across the perimeter of the drop, particularly along the directions parallel and perpendicular to the 1D surface roughness. We also examined the droplet contact angle anisotropy for intrinsic wettability ( $\theta_Y^W = 62^\circ$ ), previously reported by Chung *et al.*,<sup>34</sup> for details see Fig. S4. The results were consistent with  $\alpha_0$  increases from 1 to 1.4.

Fig. 3(a)–(d) illustrates the anisotropy in droplet radius ( $\alpha_R$ ) which correlates with the anisotropy in apparent contact angle ( $\alpha_0$ ). The relationship is further tested by examining the correlation plots for  $\alpha_R$ – $\alpha_0$  for varying  $A$  and  $\theta_Y^W$ , as shown in Fig. 3(e) and (f), respectively. The linear variation, *i.e.*,  $\alpha_R(A)|_{\theta_Y^W} \sim \alpha_0(A)|_{\theta_Y^W}$  and  $\alpha_R(\theta_Y^W)|_A \sim \alpha_0(\theta_Y^W)|_A$  is apparent, further confirming

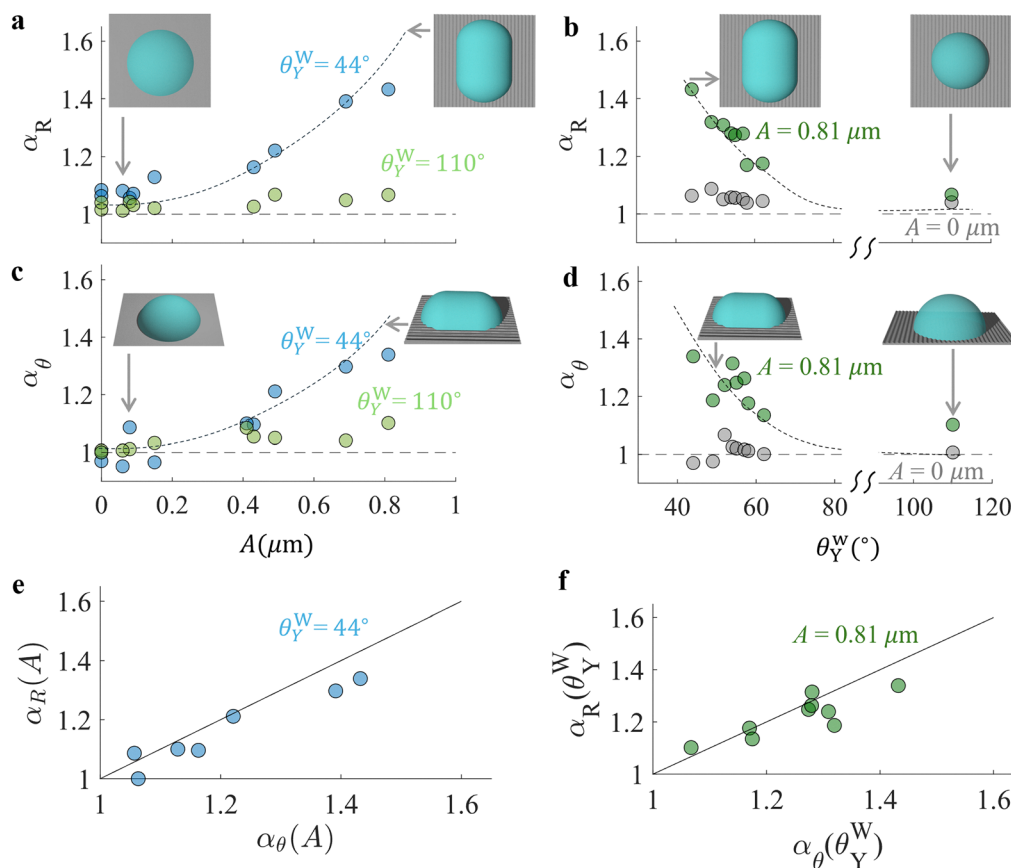


**Fig. 3** Droplet anisotropy  $\alpha_R = R_{\parallel}/R_{\perp}$  and  $\alpha_{\theta} = \theta_{\perp}/\theta_{\parallel}$  on planar ( $A = 0$ ) and rough ( $A \neq 0$ ) surfaces under hydrophilic ( $\theta_Y^W = 44^\circ$ ) and hydrophobic ( $\theta_Y^W = 110^\circ$ ) conditions. (a) and (c) Plots of anisotropy ratios  $\alpha_R$  and  $\alpha_{\theta}$  as functions of roughness amplitude  $A$  for  $\theta_Y^W = 44^\circ$  and  $\theta_Y^W = 110^\circ$ , respectively. Increasing  $A$  induces greater anisotropy, with values rising from 1 to 1.4, indicating a transition from circular to non-circular droplet shapes. (b) and (d) Plots of  $\alpha_R$  and  $\alpha_{\theta}$  versus intrinsic contact angle  $\theta_Y^W$  for roughness amplitudes  $A = 0$  and  $A = 0.81 \mu\text{m}$ , respectively. As  $\theta_Y^W$  increases, anisotropy decreases from 1.4 to 1.0, signifying a shift from non-circular to circular droplet shapes. Each datum represents an average of three spatial measurements on the substrate, with typical variation of  $\pm 0.1$  in  $\alpha_R$  and  $\alpha_{\theta}$ . The dashed line at  $\alpha_R = 1 = \alpha_{\theta}$  denotes a circular droplet, a representative ideal case for a droplet on a planar surface. The schematic images show the top and side views of water droplets (circular – elongated shapes and symmetric to non-symmetric apparent contact angles) corresponding to high and low  $\alpha_R = (1, 1.4)$  and  $\alpha_{\theta} = (1, 1.4)$  are highlighted. (e) and (f) Correlation plot between  $\alpha_R(A)$  and  $\alpha_{\theta}(A)$  for  $\theta_Y^W = 44^\circ$ , and between  $\alpha_R(\theta_Y^W)$  and  $\alpha_{\theta}(\theta_Y^W)$  for  $A = 0.81 \mu\text{m}$ , respectively. The dotted lines as indicated in (a)–(f) are guide to the eye.

that the anisotropy in droplet radii is followed by anisotropy in apparent contact angles.

### 3.2 Directional droplet motion on vertically inclined surfaces

To investigate the influence of the droplet shape anisotropy on the kinetic motion across the surface with microwrinkles, we examine droplet displacement along the direction parallel to the surface wrinkles on vertically inclined substrates. The objective is to determine how the specific combinations of roughness amplitude ( $A$ ) and intrinsic contact angle ( $\theta_Y^W$ ) promote spontaneous droplet removal under gravity. Experiments were carried out at the extremes of the parameter space tested: roughness amplitudes of  $A = 0$  and  $0.81 \mu\text{m}$ , and intrinsic contact angles of  $\theta_Y^W = 62^\circ$  and  $110^\circ$ , as shown in Fig. 4.

Fig. 4(a) and (b) present time-lapse top-view images of  $6 \mu\text{L}$  water droplets on vertically inclined PDMS surfaces with microwrinkles with amplitude  $A = 0.81 \mu\text{m}$  and intrinsic contact angles of  $\theta_Y^W = 62^\circ$  and  $110^\circ$ , respectively. As previously observed, at  $\theta_Y^W = 62^\circ$ , the droplet exhibits the elongated

shape along the wrinkle direction and undergoes vertical displacement, which was recorded during the time interval of 12 seconds. In contrast, at  $\theta_Y^W = 110^\circ$ , the droplet maintains a circular footprint and remains stationary throughout the observation period, indicating that hydrophobicity suppresses motion, even in the presence of surface wrinkles (see Movies M1 and M3).

Fig. 4(c) and (d) show analogous experiments on smooth PDMS surfaces ( $A = 0 \mu\text{m}$ ) with  $\theta_Y^W = 62^\circ$  and  $110^\circ$ , respectively. In both cases, the droplet remains circular and static, reflecting the behaviour observed for the wrinkled surface at  $\theta_Y^W = 110^\circ$  (see Fig. 4(b)). These observations indicate that droplet mobility on vertically inclined surfaces is not solely governed by the presence of 1D microwrinkles. Instead, it is the combined effect of wrinkling amplitude ( $A$ ) and moderate wettability (lower  $\theta_Y^W$ ) that gives rise to shape anisotropy, an essential factor allowing gravity-driven motion along the wrinkle direction.

To further quantify the motion of droplets, we tracked the centroid of a droplet over time, varying from  $t = 0$  to  $t = 12$



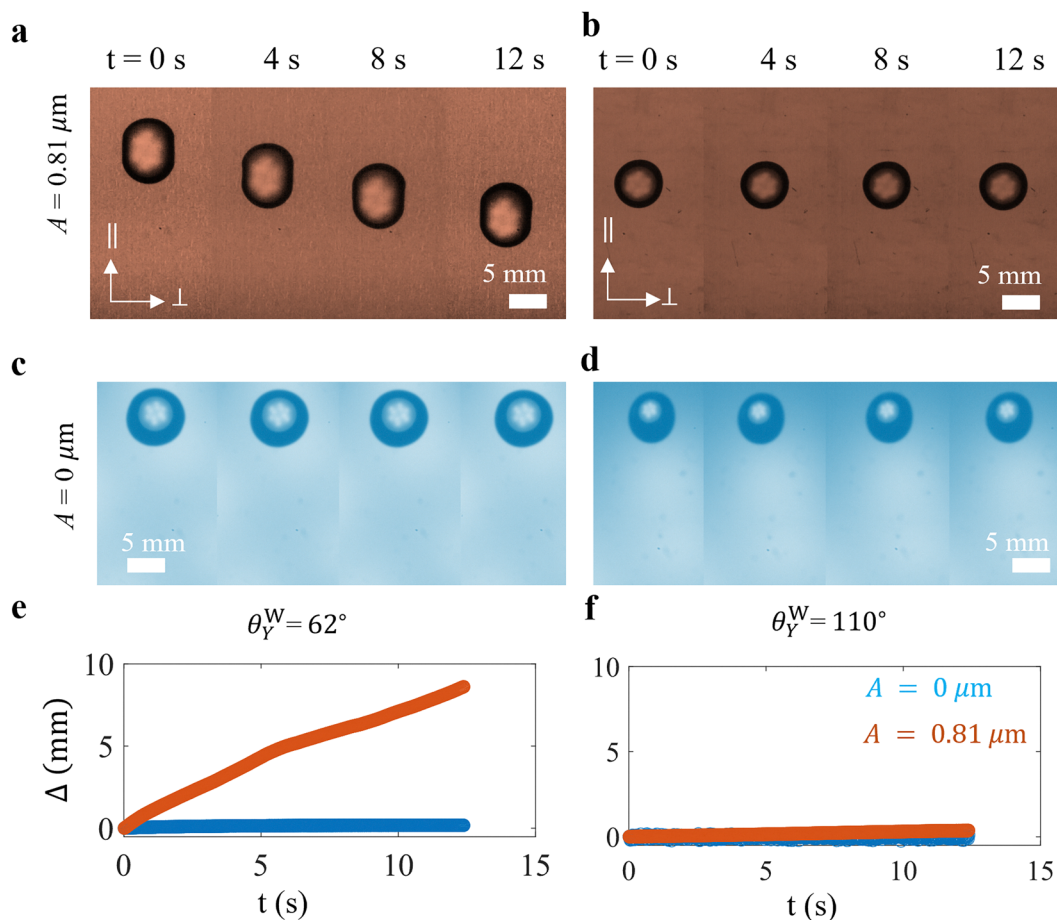


**Fig. 4** Directional sliding of 6  $\mu\text{L}$  water droplets on vertically inclined planar ( $A = 0$ ) and wrinkled ( $A = 0.81 \mu\text{m}$ ) surfaces under hydrophilic ( $\theta_Y^W = 62^\circ$ ) and hydrophobic ( $\theta_Y^W = 110^\circ$ ) conditions. (a) and (b) Time-lapse top-view images of droplet motion on wrinkled surfaces for  $\theta_Y^W = 62^\circ$  and  $\theta_Y^W = 110^\circ$ , respectively. (c) and (d) Corresponding images on planar surfaces under the same wettability conditions. The directions parallel ( $\parallel$ ) and perpendicular ( $\perp$ ) to the wrinkle orientation are indicated. (e) and (f) Displacement of the droplet centroid  $\Delta$  along the  $\parallel$  direction for different  $A$  as a function of time  $t$ , for (e)  $\theta_Y^W = 62^\circ$  and (f)  $\theta_Y^W = 110^\circ$ . Significant droplet mobility is observed only in the  $\parallel$  direction on wrinkled surfaces, with no motion along  $\perp$  under moderately hydrophilic properties (see Movies S1 and S2). In all other cases, the droplet remains stationary within the observed time interval. Linear fit to  $\Delta$ – $t$  shown in (e) for  $A = 0.81 \mu\text{m}$  and  $A = 0 \mu\text{m}$  yields a slope  $0.81 \text{ mm s}^{-1}$ , and  $0.03 \text{ mm s}^{-1}$ , the slope corresponding to sliding velocity,  $v$ . Similarly, linear fit to  $\Delta$ – $t$  shown in (f), corresponding to  $A = 0.81 \mu\text{m}$  and  $A = 0 \mu\text{m}$  yields a slope of  $0.03 \text{ mm s}^{-1}$  and  $0.01 \text{ mm s}^{-1}$ .

seconds. Fig. 4(e) and (f) plot the time-dependent displacement for  $\theta_Y^W = 62^\circ$  and  $110^\circ$  on surfaces with  $A = 0$  and  $0.81 \mu\text{m}$ , respectively. For surfaces with microwrinkles and  $\theta_Y^W = 62^\circ$ , the displacement increases linearly with time (0–12 seconds), indicating constant velocity and sustained motion. In contrast, for all other cases, including surfaces with and without microwrinkles, at  $\theta_Y^W = 110^\circ$ , we did not observe any measurable displacement, confirming that the droplets were effectively static (see Movies M3–M5 in the SI). Furthermore, the droplet on a vertically inclined surface with  $\theta_Y^W = 62^\circ$  and surface wrinkle perpendicular to the direction of gravity was observed to be stationary during 12 seconds, as shown in Fig. S5. This indicates that for a given droplet volume, the resistance for the droplet motion is higher in the perpendicular direction than in the parallel direction.

For completion, we verified our observations of droplet sliding on the wrinkled surface with low wettability ( $\theta_Y^W = 22^\circ$ ). The sliding onset volume was  $2 \mu\text{L}$  when the wrinkles were oriented parallel to gravity, whereas a  $2 \mu\text{L}$  droplet remained stationary when

the wrinkles were oriented perpendicular to gravity. In such low wettability surface, as expected<sup>44</sup> capillarity effects play a significant role, and liquid filaments imbibe through into the troughs of the microwrinkles. Otherwise, the droplet behaviour is analogous to that observed at  $\theta_Y^W = 62^\circ$ , as detailed in Fig. S6.

## 4 Discussion

The results presented above demonstrate a strong coupling between surface-induced anisotropy in wettability, along the directions parallel and perpendicular to surface wrinkles, and the resulting shape of sessile droplets. On the PDMS surfaces with 1D microwrinkles, droplets undergo a distinct transition from circular to elongated footprints depending on both wrinkling amplitude ( $A$ ) and intrinsic contact angle ( $\theta_Y^W$ ). The underlying mechanism driving the droplet shape anisotropy can be interpreted through the interplay between the surface free energy of





the PDMS substrate,  $\Gamma$ , and the liquid surface tension,  $\gamma$ . The equilibrium shape of a droplet and the apparent contact angle minimises the total interfacial energy, which is influenced by both surface roughness and the surface free energy ( $\Gamma$ ). Surfaces with microwrinkles perturb the interfacial energy at the contact line, and the microwrinkle-induced roughness, resulting in uneven surface free energy, differing in  $\parallel$  and  $\perp$  to the wrinkles. For droplets contact line to spread along the direction  $\perp$  to wrinkles, a larger energy barrier has to be overcome, compared to the direction  $\parallel$  to wrinkles.<sup>34</sup> This anisotropy leads to uneven spreading and directional deformation of the droplet contact line, culminating in droplet shape anisotropy.<sup>45–47</sup> We next consider the dynamics of droplets on vertically inclined surfaces and introduce a minimal model (schematic in Fig. 5) that contrasts the motion of circular and elongated droplets.

#### 4.1. Estimating droplet motion on a vertical surface

We examine the motion of droplets with elongated (non-circular) and circular contact lines (schematic in Fig. 5), sliding under gravity by balancing the driving force ( $F_g$ ) against the resistive forces, *viz.*, capillary force driven pinning ( $F_{\text{cap}}$ ) and viscous drag ( $F_{\text{drag}}$ ), that prevent sliding. The definitions of each force term are provided in the Appendix, and we thus write the force balance equation for the droplet as,

$$F = \rho V \dot{v} = \underbrace{\rho V g}_{F_g} - \underbrace{2\sqrt{R_{\perp} R_{\parallel}} \gamma (\cos \theta_b - \cos \theta_f)}_{F_{\text{cap}}} - \underbrace{2\xi \eta v R_{\perp}}_{F_{\text{drag}}} \quad (3)$$

where  $R_{\parallel}$  denotes the droplet footprint length along the direction of motion,  $\xi$  is a dimensionless damping factor,  $v$  is instantaneous sliding-velocity of a droplet,  $\gamma$  is the surface tension, and  $\eta$  represents the fluid viscosity, as illustrated in Fig. 5. We do not explicitly account for the wrinkling amplitude

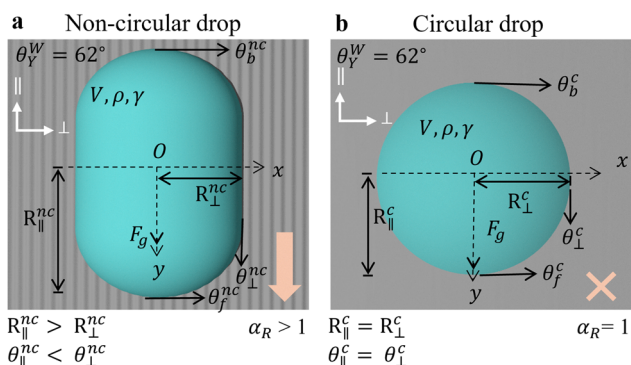


**Fig. 5** Schematic of droplets on vertically inclined wrinkled surfaces representing the scenario with  $\theta_Y^W = 62^\circ$ : (a) non-circular and (b) circular shapes. The coordinate axes ( $x$ – $y$ ) are centred at the droplet centroid  $O$ , with gravitational force  $F_g$  acting along the  $y$ -axis (parallel to wrinkle orientation). Base radii ( $R_{\parallel}$ ,  $R_{\perp}$ ), apparent contact angles ( $\theta_{\parallel}$ ,  $\theta_{\perp}$ ), and front ( $\theta_f$ ) and back ( $\theta_b$ ) apparent contact angles are indicated. The superscripts  $c$  and  $nc$  in the respective variables correspond to the circular and noncircular drops. Non-circular droplets exhibit  $R_{\parallel}^{nc} > R_{\perp}^c$  and  $\theta_{\parallel}^{nc} > \theta_{\parallel}^c$ ; circular droplets show  $R_{\parallel}^c = R_{\perp}^c$  and  $\theta_{\parallel}^c = \theta_{\perp}^c$ . The coloured arrow and cross indicate the droplet sliding or non-sliding condition, respectively. Droplet volume  $V$ , density  $\rho$ , and surface tension  $\gamma$  are also noted, along with wrinkle orientations  $\parallel$  and  $\perp$ .

**Table 1** Onset droplet sliding volumes ( $V_o^{\text{exp}}, V_o^{\text{cal}}$ ) for different surfaces and  $\theta_Y^W$ , with superscripts 'exp' and 'cal' denoting the experimentally measured and calculated values, respectively. The details in the table are for the vertically inclined substrates with droplet sliding parallel to the wrinkle orientation

$\theta_Y^W$	$A$ (mm)	$\theta_b, \theta_f$	$\alpha_R$	$2R_{\perp}$ (mm)	$V_o^{\text{exp}}$ ( $\mu\text{L}$ )/ $V_o^{\text{cal}}$ ( $\mu\text{L}$ )
$62^\circ$	0.81	$55^\circ, 63^\circ$	$\approx 1.2$	$\approx 6$ mm	$6 \mu\text{L}/\approx 6 \mu\text{L}$
$62^\circ$	0	$51^\circ, 68^\circ$	$\approx 1.0$	$\approx 6$ mm	$10 \mu\text{L}/\approx 11 \mu\text{L}$
$110^\circ$	0.81	$68^\circ, 109^\circ$	$\approx 1.0$	$\approx 5$ mm	$27 \mu\text{L}/\approx 25 \mu\text{L}$
$110^\circ$	0	$66^\circ, 109^\circ$	$\approx 1.0$	$\approx 5$ mm	$27 \mu\text{L}/\approx 26 \mu\text{L}$

(A) and the intrinsic wettability,  $\theta_Y^W$ , and instead analyse where the droplet is circular *versus* elongated, which is related to  $A$  and  $\theta_Y^W$ . We estimate the optimum volume  $V_o$ , by setting  $v = 0$ , eqn (3), corresponding to the onset of droplet sliding when the gravitational driving force becomes dominant. We neglect the inertia term ( $\dot{v} \approx 0$ ) as the Weber number  $We \ll 1$  (see the appendix for details), and obtain:

$$V_o^{\text{cal}} = \frac{2R_{\perp}\gamma}{\rho g} (\cos \theta_b - \cos \theta_f) \sqrt{\alpha_R} \quad (4)$$

where, for our system  $\alpha_R \in [1, 1.6]$  and  $(\cos \theta_b - \cos \theta_f) \in [0, 1]$ . Therefore, it is apparent from eqn (4) that the threshold volume  $V_o$ , above which the contact line begins to slide, depends on the static shape of the droplet, the characteristic radii ( $R_{\perp}$ ,  $R_{\parallel}$ ,  $\alpha_R$ ), and the apparent contact angles  $\cos \theta_b, \cos \theta_f$ . Here,  $\theta_b$  and  $\theta_f$  are the apparent contact angles of the back and front ends of a drop on a vertically inclined surface. For water droplet ( $\gamma = 72 \text{ mN m}^{-1}$ ,  $\rho = 1000 \text{ kg m}^{-3}$ ,  $g = 9.8 \text{ m s}^{-2}$ ), the threshold volume scales as  $V_o^{\text{cal}} \sim 2R_{\perp}\sqrt{\alpha_R} \times 7.2 \times 10^3 \times (\cos \theta_b - \cos \theta_f) \mu\text{L}$ .

In Table 1, we illustrate the data for the optimum volumes, both experimentally measured ( $V_o^{\text{exp}}$ ) and estimated ( $V_o^{\text{cal}}$ ) using the expression  $V_o^{\text{cal}} \sim 2R_{\perp}\sqrt{\alpha_R} \times 7.2 \times 10^3 \times (\cos \theta_b - \cos \theta_f) \mu\text{L}$ , where  $R_{\perp}$ ,  $\theta_b, \theta_f$  and  $\alpha_R$  are taken from the experimental observation. It is evident from Table 1 that the optimum volume required for sliding a circular drop ( $\alpha_R \approx 1$ ) is higher for a circular droplet than for a non-circular droplet ( $\alpha_R > 1$ ). In Table 1, we consider the simple case of sliding parallel to the wrinkle orientation.

For low intrinsic wettability, like ( $\theta_Y^W = 62^\circ$ ), the width of a circular droplet is larger than that of an elongated or noncircular (nc) drop, implying  $R_{\perp}^c > R_{\perp}^{nc}$ , follows that the optimum volume required for sliding is higher for a circular droplet than for a non-circular droplet as illustrated in Table 1.

This corroborates our experimental observation shown in Fig. 4(a) and (c), where at a given droplet volume of  $6 \mu\text{L}$ , the non-circular droplet slides while the circular one remains stationary. Similarly, for high intrinsic contact angle, like  $\theta_Y^W = 110^\circ$  for both wrinkled and non-wrinkled surfaces, as droplets are circular with  $\alpha_R = 1$  and  $R_{\perp}^c \approx R_{\perp}^{nc}$ , threshold volumes for both cases are approximately equal, corroborating the experimental observation shown in Fig. 4(b) and (d). Relative variations in velocity for circular and non-circular droplets are estimated theoretically in the SI.

For droplet sliding along the perpendicular direction, on a wrinkled surface with  $A = 0.81 \mu\text{m}$ ,  $\theta_Y^W = 62^\circ$  has  $\theta_b = 50^\circ$ ,  $\theta_f = 76^\circ$  and  $\alpha_R = 0.8$ , yielding a calculated optimum volume  $V_o^{\text{cal}} \approx 20 \mu\text{L}$ , which is close to experimentally measured  $V_o^{\text{exp}} \approx 20 \mu\text{L}$ . On a similar type surface with  $A = 0.81 \mu\text{m}$ , but with  $\theta_Y^W = 110^\circ$ ,





droplet remains circular and the optimum volumes are  $V_o^{\text{exp}} \simeq 30 \mu\text{L}$  and  $V_o^{\text{cal}} \simeq 27 \mu\text{L}$ , respectively. These estimates indicate that, even for a non-circular droplet, the potential barrier for sliding perpendicular to the wrinkle orientation is higher than that for sliding parallel, as reflected by the larger onset volume in the former case compared to the latter.

## 5 Conclusion

In summary, we systematically investigated how one-dimensional (1D) microwrinkles and intrinsic wettability influence the morphology of droplet contact line and their motion. On hydrophilic substrates with low intrinsic contact angles ( $\theta_Y^W \sim 44^\circ$ ), droplets exhibit anisotropic spreading, with footprints elongating along the direction of surface wrinkles. In contrast, on hydrophobic substrates ( $\theta_Y^W \sim 110^\circ$ ), droplets retain an isotropic circular footprint, as the contact line remains largely undeformed and the apparent contact angle is uniform. Most importantly, droplet shape anisotropy enables directional motion under gravity on vertically inclined surfaces. The elongated droplet slides at volumes for which the circular droplet remains stationary, highlighting the existence of a droplet shape-dependent threshold volume, which is relevant for the development of strategies for passive droplet transport. These findings provide a framework to describe anisotropic wetting, in terms of intrinsic surface wetting and topography, and design guidelines for functional surfaces that exploit patterning for droplet self-removal or retention.

## Conflicts of interest

There are no conflicts to declare.

## Data availability

The data supporting this article have been included as part of the SI. The details of the data and the supplementary videos are provided in the Supplementary Information. See DOI: <https://doi.org/10.1039/d5sm00525f>

Videos of droplet motion on vertically inclined surfaces are provided.

## Appendix

### Minimal model for droplet sliding

The force balance for a droplet sliding on a surface can be expressed as

$$\underbrace{\rho V \dot{v}}_{F_{\text{in}}} = \underbrace{\rho V g}_{F_g} - \underbrace{2\sqrt{R_{\perp} R_{\parallel}} \gamma (\cos \theta_b - \cos \theta_f)}_{F_{\text{cap}}} - \underbrace{2\zeta \eta v R_{\perp}}_{F_{\text{drag}}} \quad (5)$$

### Approximations

(i) Inertia force,  $F_{\text{in}}$ : since the Weber number of the droplet ( $We = \frac{2\rho v^2 R_{\parallel}}{\gamma} \sim 10^{-5}$ ) is small, representing, inertial forces

are negligible compared to surface tension forces, and we thus approximate  $\dot{v} \approx 0$ . Therefore, the right-hand side of eqn (5) is approximated to zero.

(ii) Gravitational force,  $F_g$ : since bond number ( $Bo = \rho g V / 4R_{\parallel} R_{\perp} \gamma \sim 2.8$ ), the gravitational force is of comparable magnitude to the surface tension force.

(iii) Capillary force,  $F_{\text{cap}}$ : since the capillary number ( $Ca = v\eta / \gamma \sim 10^{-6}$ ), the surface tension force dominates over the viscous force.

(iv) Drag force,  $F_{\text{drag}}$ : assuming that the drag force arises from velocity gradients within the droplet, such that the fluid at the droplet-substrate interface satisfies the no-slip boundary condition. Thus, the resulting expression for the viscous drag force is given by:<sup>47,48</sup>

$$F_{\text{drag}} = - \int_A \tau(y) dA \approx -2\pi R_{\perp} \int C_d \eta \frac{\partial v}{\partial y} dy \simeq -2\pi R_{\perp} \int C_d \eta v \frac{dy}{y} \quad (6)$$

$$F_{\text{drag}} = -2\pi R_{\perp} C_d \eta v \left[ \int_{R_{\parallel}}^{\delta_f} \frac{dy}{y} + \int_{\delta_b}^{R_{\parallel}} \frac{dy}{y} \right] \quad (7)$$

$$= -2\pi R_{\perp} C_d \eta v \ln \frac{R_{\parallel}^2}{\delta_f \delta_b} \quad (8)$$

In the above,  $\frac{\partial v}{\partial y} \approx v/y$  in the limit  $\delta y \rightarrow 0$ ,  $C_d$  denotes the geometrical drag coefficient,<sup>47,48</sup> while  $\delta_f$  and  $\delta_b$  represent small cutoff lengths near the front and back end of contact lines, respectively, with a value  $\sim 10^{-9}$  m.<sup>15,47</sup> Note that the cutoffs, equivalent to the fluid film length, are introduced to prevent divergence at the contact lines. We set the geometric drag coefficient to  $C_d = 1$ ,<sup>47,48</sup> and equating the drag forces,  $F_d = -2\zeta \eta v R_{\perp}$ ,

$$2\zeta \eta v R_{\perp} = 2\pi R_{\perp} \eta v \ln \frac{R_{\parallel}^2}{\delta_f \delta_b} \quad (9)$$

yields a damping factor,

$$\zeta = \frac{\pi R_{\perp}}{R_{\parallel}} \ln \frac{R_{\parallel}^2}{\delta_f \delta_b} = \pi \ln \frac{R_{\parallel}}{\delta_f \delta_b} \quad (10)$$

## Acknowledgements

We acknowledge funding from the European Union (HORIZON-CL4-2021-RESILIENCE-01-20) underwritten by UKRI (InnovateUK 10042469) for the Triple-A-COAT consortium. JTC thanks the EPSRC (EP/V056891/1) and the Royal Academy of Engineering (RCSRF1920/10/60) for funding a Research Chair. We acknowledge Ronojoy Adhikari (DAMTP, Cambridge) for useful discussions.

## References

- 1 K.-C. Park, H. J. Choi, C.-H. Chang, R. E. Cohen, G. H. McKinley and G. Barbastathis, *ACS Nano*, 2012, **6**, 3789–3799.
- 2 J. Shi, L. Xu and D. Qiu, *Adv. Sci.*, 2022, **9**, 2200072.



- 3 Y. Chen, Z. Quan, P. Wang, X. Zhang, H. Ding, B. Li, B. Li, S. Niu, J. Zhang and Z. Han, *et al.*, *ACS Appl. Mater. Interfaces*, 2024, **16**, 65656–65666.
- 4 G. Wang, F. Ma, L. Zhu, P. Zhu, L. Tang, H. Hu, L. Liu, S. Li, Z. Zeng and L. Wang, *et al.*, *Adv. Mater.*, 2024, **36**, 2311489.
- 5 D. Boylan, D. Monga, Z. Guo, P. S. Dosawada, L. Shan, P. Wang and X. Dai, *Adv. Funct. Mater.*, 2024, **34**, 2400194.
- 6 F. Wang, Y. Wu and B. Nestler, *Adv. Mater.*, 2023, **35**, 2210745.
- 7 F. Box, C. Thorogood and J. Hui Guan, *J. R.Soc., Interface*, 2019, **16**, 20190323.
- 8 D. Yang, A. Ramu and D. Choi, *npj Clean Water*, 2024, **7**, 20.
- 9 N. Xue, L. A. Wilen, R. W. Style and E. R. Dufresne, *Soft Matter*, 2025, **21**, 209–215.
- 10 J. Li, S. Yu, Q. Feng, F. Du, X. Du and L. Ren, *Adv. Eng. Mater.*, 2023, **25**, 2201704.
- 11 K. Smith-Mannschott, Q. Xu, S. Heyden, N. Bain, J. H. Snoeijer, E. R. Dufresne and R. W. Style, *Phys. Rev. Lett.*, 2021, **126**, 158004.
- 12 G. Hassan, B. S. Yilbas, A. Al-Sharafi and H. Al-Qahtani, *Sci. Rep.*, 2019, **9**, 5744.
- 13 F. J. Dent, G. Tyagi, F. Esat, J. T. Cabral and S. Khodaparast, *Adv. Funct. Mater.*, 2024, **34**, 2307977.
- 14 J. Lou, S. Shi, C. Ma, X. Zhou, D. Huang, Q. Zheng and C. Lv, *Nat. Commun.*, 2022, **13**, 2685.
- 15 P.-G. De Gennes, *Rev. Mod. Phys.*, 1985, **57**, 827.
- 16 D. Xia, L. M. Johnson and G. P. López, *Adv. Mater.*, 2012, **24**, 1287–1302.
- 17 D. Rhee, W.-K. Lee and T. W. Odom, *Angew. Chem.*, 2017, **129**, 6623–6627.
- 18 M. A. Quetzeri-Santiago, A. A. Castrejón-Pita and J. R. Castrejón-Pita, *Sci. Rep.*, 2019, **9**, 15030.
- 19 A. Naga, A. Kaltbeitzel, W. S. Wong, L. Hauer, H.-J. Butt and D. Vollmer, *Soft Matter*, 2021, **17**, 1746–1755.
- 20 S. Perumanath, R. Pillai and M. K. Borg, *Nano Lett.*, 2023, **23**, 4234–4241.
- 21 J. Schmid, T. Armstrong, F. J. Dickhardt, S. R. Iqbal and T. M. Schutzius, *Sci. Adv.*, 2023, **9**, eadj0324.
- 22 Y. Yao, R. K. Bennett, Y. Xu, A. M. Rather, S. Li, T. C. Cheung, A. Bhanji, M. J. Kreder, D. Daniel and S. Adera, *et al.*, *Proc. Natl. Acad. Sci. U. S. A.*, 2022, **119**, e2211042119.
- 23 J. Lu, X. Chen, X. Ding, Z. Jia, M. Li, M. Zhang, F. Liu, K. Tang, X. Yu and G. Li, *Adv. Sci.*, 2024, **11**, 2401940.
- 24 H. Lama, M. G. Basavaraj and D. K. Satapathy, *Soft Matter*, 2017, **13**, 5445–5452.
- 25 H. Lama, D. K. Satapathy and M. G. Basavaraj, *Langmuir*, 2020, **36**, 4737–4744.
- 26 Z. Cheng, D. Zhang, T. Lv, H. Lai, E. Zhang, H. Kang, Y. Wang, P. Liu, Y. Liu and Y. Du, *et al.*, *Adv. Funct. Mater.*, 2018, **28**, 1705002.
- 27 J. Bico, C. Tordeux and D. Quéré, *Europhys. Lett.*, 2001, **55**, 214.
- 28 P.-G. De Gennes, F. Brochard-Wyart and D. Quéré, *Capillarity and wetting phenomena: drops, bubbles, pearls, waves*, Springer Science & Business Media, 2003.
- 29 D. Quéré, *Annu. Rev. Mater. Res.*, 2008, **38**, 71–99.
- 30 S. Herminghaus, M. Brinkmann and R. Seemann, *Annu. Rev. Mater. Res.*, 2008, **38**, 101–121.
- 31 D. Bonn, J. Eggers, J. Indekeu, J. Meunier and E. Rolley, *Rev. Mod. Phys.*, 2009, **81**, 739–805.
- 32 M. Morita, T. Koga, H. Otsuka and A. Takahara, *Langmuir*, 2005, **21**, 911–918.
- 33 H. Kusumaatmaja, J. Leopoldes, A. Dupuis and J. Yeomans, *Europhys. Lett.*, 2006, **73**, 740.
- 34 J. Y. Chung, J. P. Youngblood and C. M. Stafford, *Soft Matter*, 2007, **3**, 1163–1169.
- 35 H. Jiang, D.-Y. Khang, J. Song, Y. Sun, Y. Huang and J. A. Rogers, *Proc. Natl. Acad. Sci. U. S. A.*, 2007, **104**, 15607–15612.
- 36 M. Ouyang, R. Muisener, A. Boulares and J. Koberstein, *J. Membr. Sci.*, 2000, **177**, 177–187.
- 37 K. Efimenko, W. E. Wallace and J. Genzer, *J. Colloid Interface Sci.*, 2002, **254**, 306–315.
- 38 A. Oláh, H. Hillborg and G. J. Vancso, *Appl. Surf. Sci.*, 2005, **239**, 410–423.
- 39 A. Chiche, C. M. Stafford and J. T. Cabral, *Soft Matter*, 2008, **4**, 2360–2364.
- 40 S. Cai, D. Chen, Z. Suo and R. C. Hayward, *Soft Matter*, 2012, **8**, 1301–1304.
- 41 J. Zang, X. Zhao, Y. Cao and J. W. Hutchinson, *J. Mech. Phys. Solids*, 2012, **60**, 1265–1279.
- 42 D. Qin, Y. Xia and G. M. Whitesides, *Nat. Protoc.*, 2010, **5**, 491.
- 43 M. Nania, F. Foglia, O. K. Matar and J. T. Cabral, *Nanoscale*, 2017, **9**, 2030–2037.
- 44 K. Khare, J. Zhou and S. Yang, *Langmuir*, 2009, **25**, 12794–12799.
- 45 É. Lorenceau, C. Clanet and D. Quéré, *J. Colloid Interface Sci.*, 2004, **279**, 192–197.
- 46 T. Gilet, D. Terwagne and N. Vandewalle, *Eur. Phys. J. E:Soft Matter Biol. Phys.*, 2010, **31**, 253–262.
- 47 M. Leonard, J. Van Hulle, F. Weyer, D. Terwagne and N. Vandewalle, *Phys. Rev. Fluids*, 2023, **8**, 103601.
- 48 X. Li, F. Bodziony, M. Yin, H. Marschall, R. Berger and H.-J. Butt, *Nat. Commun.*, 2023, **14**, 4571.

